Chemical Science

EDGE ARTICLE

Nanoconfinement-induced high-rate performance of hard carbon for densified sodium cluster storage

Lian Chen,†[ab] Fan Li,†[b] Kaiyang Liu,[b] Feng Wang, [ID][a] Zhengshuai Bai,*[b] Yanyan Zhang [ID] [b] and Yuxin Tang [ID] *[ab]

Hard carbon is recognized as a promising anode material for sodium-ion batteries, but its practical application is constrained by low initial Coulombic efficiency (ICE), insufficient reversible capacity, and poor rate performance, which are rooted in inadequate pseudo-graphitic domain structure and uncontrolled sodium cluster formation. Herein, we propose a nanoconfinement strategy *via* graphene orientation-guided graphitization to achieve high-rate performance of cellulose-derived hard carbon. The oxygen-functional groups on graphene form a stable cross-linking structure with cellulose to suppress disordered defects, while the sp^2-hybridized carbon skeleton guides the directional arrangement of carbon layers, synergistically constructing a confined structure with abundant pseudo-graphitic domains and size-tunable closed pores. Benefiting from this optimized structure, the resultant electrode achieves a high specific capacity of 323.9 mAh g^{-1}, an ICE of 89.9%, and excellent rate performance (226.8 mAh g^{-1} at 3.0 A g^{-1}). More importantly, sodium metal clusters are for the first time observed *via* nanoconfinement induction with the filling stage achieving their controllable densification through enhanced micropore confinement. This further validates and reinforces the new adsorption–intercalation–pore filling mechanism for sodium cluster densification. This work highlights nanoconfinement induction for high-rate hard carbon anodes, promoting the application of sodium-ion batteries in large-scale energy storage systems.

Introduction

Sodium-ion batteries (SIBs) are increasingly regarded as a sustainable alternative to lithium-ion batteries, especially for large-scale and grid-level energy storage systems.[1,2] Among various anode materials, hard carbon is widely recognized as one of the most promising candidates for SIB anodes, with several advantages such as high theoretical capacity, good cycling stability, and relatively low cost.[3,4] However, hard carbon features a structure consisting of irregular graphitic stacks with long-range disorder and short-range order, accompanied by a large number of edge defect sites and a randomly distributed pore network. These structural characteristics directly give rise to three critical issues: (i) low initial Coulombic efficiency (ICE) stemming from irreversible side reactions at defective surfaces,[5–8] (ii) inadequate reversible capacity due to the insufficient pseudo-graphitic domains that fail to provide abundant sodium storage sites,[9,10] and (iii) poor rate performance caused by sluggish sodium ion diffusion within disordered

structures.[11–13] The core cause of these issues is particularly evident in the low-voltage plateau region (<0.1 V), which determines high capacity—where the sodium storage mechanism is dominated by the formation of sodium metal clusters in pseudo-graphitic domains and closed pores. The uncontrolled formation and evolution of these clusters directly limit the performance improvement of hard carbon.

As a widely available and low-cost biomass precursor of cellulose, the as-obtained hard carbon exhibits an inadequate pseudo-graphitic domain region and broad size distribution of closed pores with disordered walls, resulting in a lack of effective spatial confinement during the sodium ion filling process and uncontrolled sodium metal cluster storage.[14–16] On one hand, the sodium atoms are loosely packed within certain regions of the pseudo-graphitic domains and the closed pores, making it challenging to reduce atomic spacing (*e.g.*, the Na (111) interplanar spacing fails to reach the optimal densified state). This results in a low sodium atomic density per unit pore volume, rendering the low-voltage plateau capacity typically below 200 mAh g^{-1}.[17,18] On the other hand, the randomly growing loose sodium clusters tend to aggregate across closed pore wall and pseudo-graphitic domain region boundaries, leading to incomplete decomposition of clusters during the cycling process and continuous accumulation of irreversible capacity loss and reduced ICE.[19–21] Additionally, the abundant

*a*Qingyuan Innovation Laboratory, 1 Xueyuan Road, Quanzhou 362801, P. R. China. E-mail: yxtang@fzu.edu.cn

*b*College of Chemical Engineering, Fuzhou University, Fuzhou 350116, P. R. China. E-mail: baizs@fzu.edu.cn

† These authors contributed equally to this work.

pseudo-graphitic domains form continuous interconnected sodium-ion transport channels, significantly lowering ion migration energy barriers, accelerating transport kinetics, and boosting hard carbon electrode structural integrity.[22–24] Thus, forcing sodium atoms to stack tightly in a limited space through spatial confinement and suppressing side reactions and structural damage caused by the disordered growth of clusters serve to increase sodium storage capacity. Accordingly, engineering controllable pseudo-graphitic domain regions and closed-pore structures is the core for realizing high-rate hard carbon electrodes with densified sodium cluster storage.

In this work, we propose a strategy of graphene orientation-induced graphitization confinement, which utilizes the differences in the roles of acidified graphene at different carbonization stages to achieve confined orientation graphitization. The aim is to construct high-rate performance hard carbon with densified sodium metal clusters and high ICE. On one hand, the oxygen functional groups on graphene form a stable cross-linked structure with cellulose molecules, suppressing the generation of disordered defects in the low-temperature stage. On the other hand, the acidified graphene with an sp^2-hybridized skeleton guides the directional arrangement of carbon layers, forming ordered channels with stable interlayer spacing and providing molecular-scale guide rails for the rapid transport of sodium ions. Meanwhile, the cross-linked network of graphene and cellulose is accompanied by gas release during carbonization, evolving into rigid closed-pore cages wrapped by directional pseudo-graphitic layers (with closed pore sizes concentrated at 0.54 nm). This spatial confinement forces sodium atoms to stack tightly within the pores. When discharged to the plateau region of the optimized hard carbon, the characteristic peaks of sodium metal clusters (23.5°, 31°) shift to higher angles, corresponding to the contraction of the Na (111) interplanar spacing, directly confirming the densified clusters. Benefiting from the nanoconfinement structure, the obtained electrode achieves an ICE of 89.9% and a specific capacity of 323.9 mAh g^{-1}, with a low-voltage plateau capacity of 216.4 mAh g^{-1}, and the capacity retention is still 80.2% after 1000 cycles, which is obviously better than that of cellulose-derived hard carbon. The proposed graphene-induced confined structure provides new insights into the densified sodium clusters of hard carbon anodes and is expected to offer strong support for the application of sodium-ion batteries in the field of large-scale energy storage.

Results and discussion

In this work, we employed acidified graphene as a structural target to mediate the formation of confined-structure type hard carbon around the pseudo-graphitic domains during the pyrolytic transformation of cellulose precursors. As shown in Fig. 1, based on the graphene orientation-induced graphitization nanoconfinement strategy, the oxygen-functional groups on acidified graphene form a stable cross-linking structure with cellulose molecules due to the hydrogen bonds and covalent bonds, inhibiting the generation of disordered defects before high-temperature carbonization. The sp^2-hybridized carbon skeleton of graphene can provide nucleation centers for the graphitization of cellulose-derived carbon, induce the ordered arrangement of carbon atoms and promote the formation of a local confined structure around the pseudo-graphitic domains in the high-temperature carbonization process. The obtained hard carbon increases the proportion of short-range ordered structures and closed pore volume, which enables densified sodium cluster storage via its confined structure. As a proof of concept, different contents of graphene (0.5%, 1%, and 2%) have been used for incorporation into cellulose and carbonization at 1300 °C for 2 h, which have been assigned as HC-G-0.5, HC-G-1 and HC-G-2. Cellulose without added graphene in the same carbonization process was named hard carbon (HC), and the hard carbon obtained directly with 1% graphene was named HC@G to verify the graphene orientation-induced
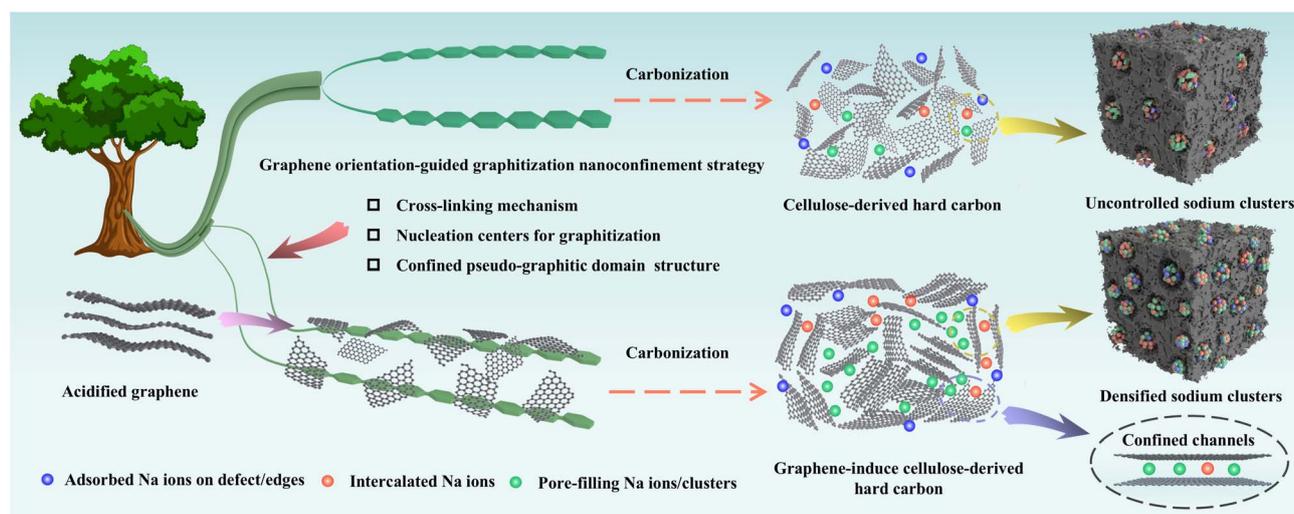

Fig. 1 Schematic images of uncontrolled sodium cluster storage by regular strategy type hard carbon and densified sodium cluster storage by confined-structure type hard carbon.

graphitization (more details in the Experimental section). Furthermore, the graphene adheres to the surface of large-sized cellulose and forms a highly cross-linked composite hard carbon precursor through mutual interweaving. During the high-temperature carbonization process, accompanied by gas release, it is further transformed into closed-pore walls, forming a critical confined structure for sodium ion transport in the low-voltage plateau region.

The SEM images demonstrate that cellulose remains fibrous after pyrolysis while graphene is attached to cellulose in a flake-like form (Fig. S1 and S2, SI) due to hydrogen bonding and cross-linking interactions. As shown in Fig. S3, SI, the as-prepared hard carbon series has blurred lattice fringes and enhanced pseudo-graphitic domains and closed pore structure. As the amount of graphene increases, more short-range pseudo-graphitic domains are formed, with their thickness increasing accordingly. The abundant pseudo-graphitic domains can form closed pores with a house-of-cards feature, providing additional sodium ion storage for hard carbon, while excessively thick pseudo-graphitic domains hinder the transport of sodium ions in the hard carbon.[25,26] It is worth noting that the HC-G-1 sample exhibits a structure where short-range graphitic layers are encapsulated by surrounding curved pseudo-graphitic domains, forming a confined structure of closed pores (rigid nanocages) embedded in the carbon matrix (Fig. 2a–d). More importantly, the unique structure created by the graphene orientation-induced strategy can both suppress excessive defect sites and provide a favorable pathway for the insertion of sodium ions. This is distinctly different from the HC@G sample, in which graphene simply overlaps the hard carbon surface (Fig. S4, SI). Additionally, compared to the other samples, the HC-G-2 sample has the thickest pseudo-graphitic domain region with a highly developed closed-pore region. As indicated in Fig. 2e, S3 and S5, SI, the XRD patterns of all samples show two peaks at $\approx 23°$ and $44°$, corresponding to the (002) and (100) crystal planes of the hard carbon. The graphene-added samples all exhibit a sharp peak at $26.5°$ corresponding to the graphene (002) crystal plane, and the intensity gradually increases with increasing amount of graphene. In addition to this change, the (002) peak of the hard carbon is also red
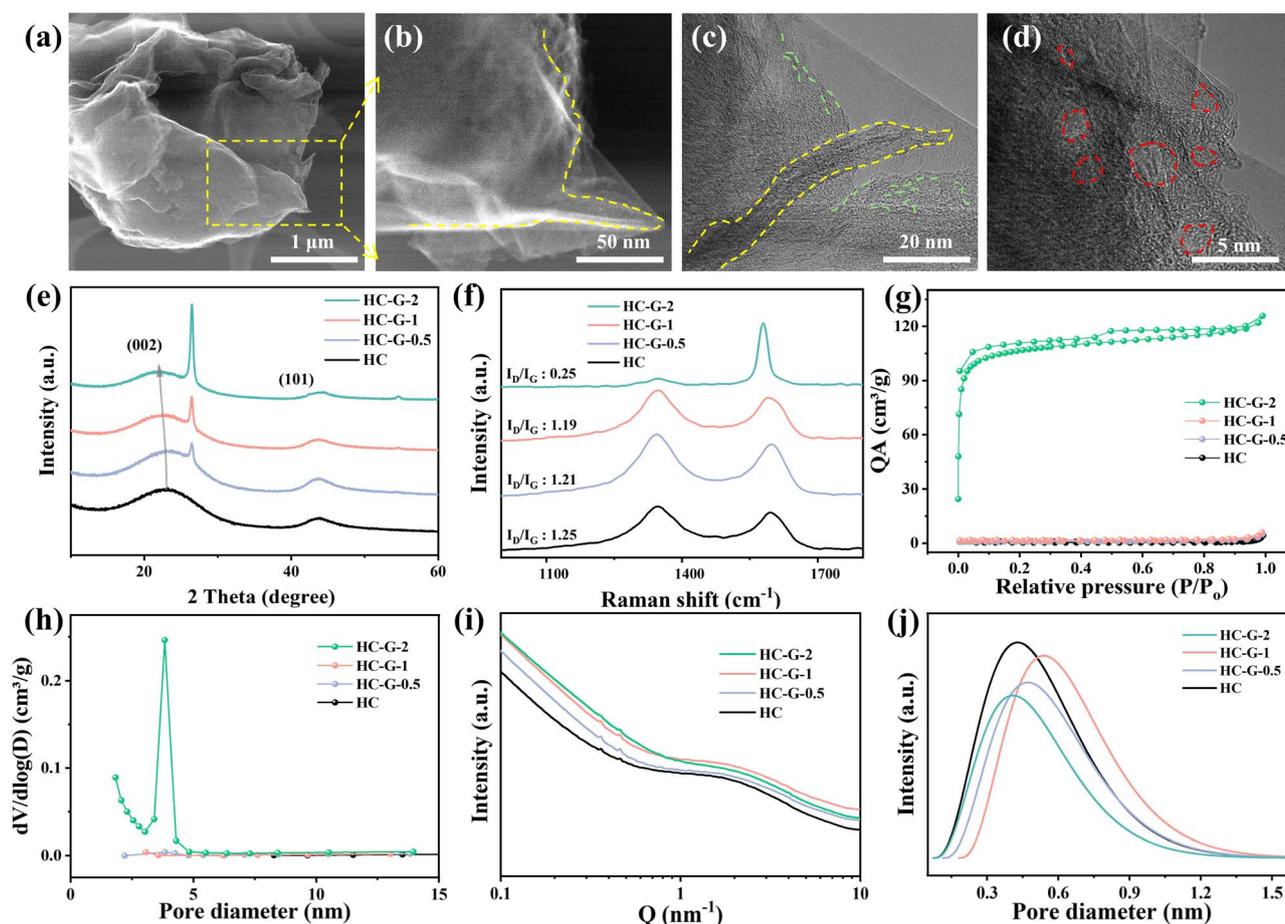

Fig. 2 Structural characterization of the graphene orientation-induced cellulose-derived hard carbon series. (a–d) The TEM images of the HC-G-1 sample with different magnifications (the yellow section indicates embedded graphene in the carbon matrix, the green section represents enlarged interlayer distance, and the red section corresponds to rigid nanocages). (e and f) The X-ray diffraction (XRD) patterns and Raman spectra of HC, HC-G-0.5, HC-G-1, and HC-G-2 samples. (g and h) The N$_2$ adsorption/desorption isotherms and pore size distribution of HC, HC-G-0.5, HC-G-1 and HC-G-2 samples. (i and j) The small angle X-ray scattering (SAXS) profiles and fitted closed-pore size distribution of HC, HC-G-0.5, HC-G-1 and HC-G-2 samples.

shifted, which is related to the high interlayer spacing of HC, HC-G-0.5, HC-G-1 and HC-G-2 calculated by Bragg's formula as 0.374, 0.386, 0.395 and 0.398 nm (Table S1, SI). Meanwhile, high-resolution transmission electron microscopy further verifies the expansion of the interlayer spacing in hard carbon. The directional arrangement between interlayers enables pre-confinement of sodium ions *via* interactions between π-electrons and sodium ions, guiding their directional migration along channels to closed pores and preventing random accumulation in disordered carbon layers that would form loose clusters.[27] In addition, we also analyzed the surface functional groups of the hard carbon precursor by Fourier-transform infrared spectroscopy. The results showed that the vibration peak of –C=O increased with the increase of graphene (Fig. S6, SI), indicating that cross-linking reactions might have formed between graphene and cellulose through hydrogen bonds and covalent bonds.[28] Raman spectroscopy reveals two broad peaks in all samples at 1350 cm^{-1} and 1580 cm^{-1}, corresponding to the D-band and G-band of the as-prepared hard carbon series, respectively.[29] The HC, HC-G-0.5, and HC-G-1 samples exhibit slight differences in the intensity between the D and G peaks (Fig. 2f), whereas the HC-G-2 sample shows an over-intense G peak and an under-intense D peak. Based on the common Raman vibrational modes of carbon materials, HC, HC-G-0.5, and HC-G-1 were fitted to four peaks (Fig. S7 and S8, SI). The ratio of the D peak (corresponding to the defective sp^2 structure) to the G peak (corresponding to ordered sp^2 carbon), denoted as I_D/I_G, is commonly used to evaluate the graphitization degree of carbon materials. The I_D/I_G values for HC, HC-G-0.5, HC-G-1, and HC-G-2 are 1.25, 1.21, 1.19, and 0.25, respectively. Notably, the I_D/I_G ratio of all samples decreases with increasing graphene addition. This result indicates that a moderate amount of graphene can regulate hard carbon to achieve a suitable graphitization degree, while excessive addition of HC-G-2 sample leads to over-graphitization of the hard carbon.

The pore structure of the obtained hard carbon series was characterized by nitrogen adsorption–desorption isotherms curves and small-angle X-ray scattering (SAXS). The nitrogen adsorption–desorption isothermal curves were typical of type IV for all samples in Fig. 2g. The specific surface areas of the HC,
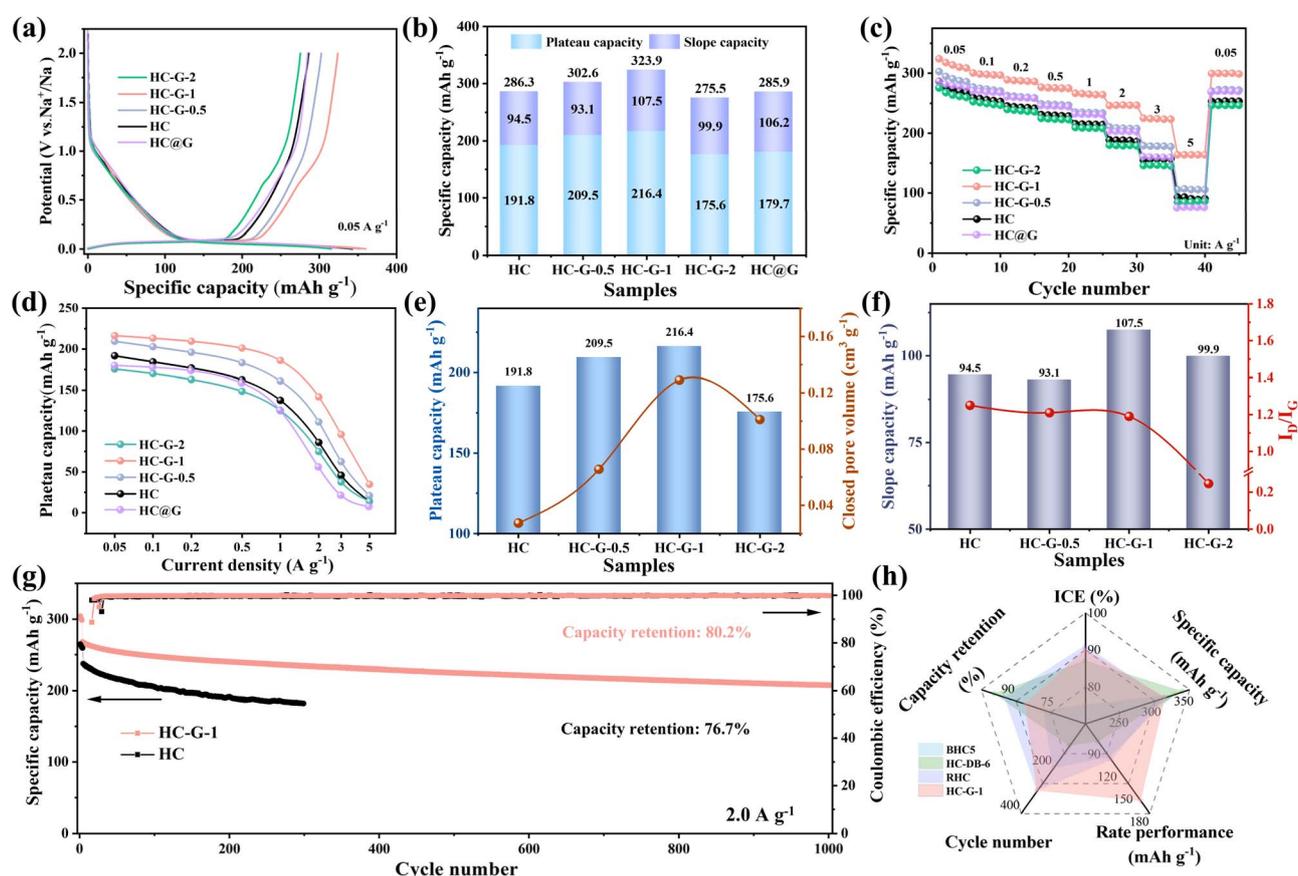

Fig. 3 Electrochemical performance of the graphene orientation-induced cellulose-derived hard carbon series. (a) The first discharge/charge curves for different samples in half cells at a current density of 0.05 A g^{-1}, (b) slope and plateau capacity of the second discharge at a current density of 0.05 A g^{-1}, and (c) rate performance of the HC, HC-G-0.5, HC-G-1, HC-G-2, and HC@G electrodes. (d) Plateau capacity of the HC, HC-G-0.5, HC-G-1, HC-G-2, and HC@G electrodes from 0.05 to 5 A g^{-1}. (e) Relationship between the closed pore volume and plateau capacity, (f) relationship between I_D/I_G and slope capacity, (g) cycling performance of the HC and HC-G-1 electrodes at a current density of 2.0 A g^{-1}, and (h) comparison of ICE, rate performance, cycle number, and capacity retention of HC-G-1 with highly relevant BHC5, HC-DB-6, and RHC hard carbon anodes.

HC-G-0.5, HC-G-1 and HC-G-2 samples were 1.17, 3.62, 5.88 and 421 m^2 g^{-1}, respectively (Table S2, SI). The specific surface areas of the HC, HC-G-0.5 and HC-G-1 samples gradually increased with the addition of graphene. However, with the continued addition of graphene, the specific surface area of the HC-G-2 sample is increased dramatically to 421 m^2 g^{-1}, which is related to the high specific surface area of graphene and exposed interfaces generated by the agglomeration of excess graphene sheets. This phenomenon is consistent with the findings reported in previous studies.[30–32] Moreover, the pore size distribution also shows that the HC-G-2 sample has the largest pore size of ∼4 nm (Fig. 2h). Since nitrogen adsorption–desorption isothermal curves can only assess open pore structures,[33–35] the closed pore structure of the hard carbon was further investigated by SAXS. All samples exhibited shoulder peaks at 1–2 nm^{-1} indicating the presence of a closed pore structure (Fig. 2i). Among them, the HC-G-1 sample has the highest intensity of shoulder peaks and closed pores. The closed pore sizes were determined by analysing the fitted shoulder peaks for several hard carbon series. As illustrated in Fig. 2j, the closed pore sizes were found to be approximately 0.42 for HC, 0.47 for HC-G-0.5, 0.54 for HC-G-1, and 0.40 nm for HC-G-2. A large closed pore size facilitates the acceleration of sodium ion transport in the low-voltage plateau region especially at high current density, which is crucial for the construction of high-rate hard carbon anodes.[26,36] Based on these combined results, graphene with a characteristic long-range structure can act as a target during the pyrolysis process, which can directionally induce local graphitization of hard carbon and form confined pseudo-graphitic domains through a cross-linking mechanism mediated by hydrogen bonds and oxygen-functional groups. This process significantly increases the interlayer spacing of hard carbon, expands the pseudo-graphitic domain regions, and reduces the defect density simultaneously.

The electrochemical performance of as-prepared hard carbon series was assessed at a current density of 0.05 A g^{-1}, consisting mainly of a slope region from 0.1 to 2.0 V and a plateau region from 0.01 to 0.1 V (Fig. 3a). The specific capacity of the HC electrode was 286.2 mAh g^{-1}, with an ICE of only 83.4%, while the HC@G electrode shows a specific capacity of 288 mAh g^{-1} and ICE of 88.8%. The specific capacities of the HC-G-0.5, HC-G-1, and HC-G-2 electrodes are 302.6, 323.9 and 275.5 mAh g^{-1} with corresponding ICE values of 85.8%, 89.9% and 85.3%, respectively. These results indicate that the graphene-induced local structure nucleation series are obviously superior to that obtained *via* mechanical mixing after carbonization of the HC@G electrode. Furthermore, the HC-G-1 electrode shows the highest slope capacity of 107.5 mAh g^{-1} and plateau capacity of 216.4 mAh g^{-1} among the samples in Fig. 3b. Notably, the HC-G-2 electrode did not exhibit the maximum ICE of ∼85.3%, which is mainly attributed to electrolyte decomposition caused by its high specific surface area. Additionally, the high content graphene of the HC-G-2 electrode induces excessive pseudo-graphitic domains that can store more sodium ions, but the large amount of graphene and reduced closed pore size impede sodium ion transport,[37,38] leading to a decline in

sodium storage capacity and rate performance. As shown in Fig. 3c, S9 and S10, SI, compared to the other samples, the HC-G-1 electrode exhibits an excellent rate performance of 226.8 mAh g^{-1} even at a high current density of 3.0 A g^{-1} (164.3 mAh g^{-1} ∼5.0 A g^{-1}). The plateau capacity is an important parameter for evaluating rate performance. Notably, the HC-G-1 electrode still maintains a remarkable plateau capacity retention of 53.1% at current densities from 0.5 to 5.0 A g^{-1}, which was higher than that of the HC electrode (33.5%) (Fig. 3d).

Furthermore, we further investigated the correlation between plateau capacity and closed pore volume, and the results showed that the plateau capacity gradually increases with the increase of closed pore volume (Fig. 3e and Table S2, SI). However, the HC-G-2 electrode did not exhibit an increased plateau capacity, which is mainly related to the reduced closed pore size that allows fewer sodium ions to enter the closed pore structure in the low-voltage plateau region. This is similar to the results reported previously.[30,39] Fig. 3f illustrates the relationship between the slope capacity and the I_D/I_G ratio of these samples. With the increase in graphene content, the variation in slope capacity is mainly regulated by the defect density and reversible oxygen-containing functional groups. First, the nucleation effect of graphene during carbonization induces the formation of hard carbon with enhanced graphitization and low cross-linking degree. Consequently, the reduced defect density corresponds to a decreased slope capacity of the HC-G-0.5 electrode. Second, with the further increase in the graphene content of the HC-G-1 electrode, the elevated cross-linking degree leads to a significant increase in C=O functional groups, thereby promoting a remarkable improvement in slope capacity. Furthermore, when graphene is added in excess to the HC-G-2 electrode, the cross-linking degree remains enhanced. However, excessive graphitization results in a decreasing trend in slope capacity. Notably, the HC-G-1 electrode achieves an optimal closed pore volume and pore size distribution, which not only provides abundant active sites for sodium ion intercalation/pore filling, but also ensures fast ion diffusion within pores. Moreover, we evaluated the cycle stability of the as-prepared HC and HC-G-1 electrodes as shown in Fig. 3g. The HC sample shows a capacity retention of 76.7% with a specific capacity of 182.1 mAh g^{-1} only after 300 cycles, while the HC-G-1 electrode reveals an improved capacity retention of 80.2% and specific capacity of 207.2 mAh g^{-1} after 1000 cycles at a current density of 2.0 A g^{-1}. More importantly, we compared several key parameters to highlight the advancement of this work. The results demonstrate improvements in the ICE, rate performance, cycle number, and capacity retention of representative hard carbon anodes (Fig. 3h).[40–42]

The sodium ion diffusion coefficient was determined through Galvanostatic Intermittent Titration Technique (GITT) measurements to elucidate the sodium storage mechanism in HC and HC-G-1 electrodes. The diffusion coefficients of sodium ions are calculated according to Fick's second law.[43–45] Both the HC-G-1 and HC electrodes demonstrated comparable voltage response profiles during charge/discharge processes in Fig. 4a. During the discharge process, the diffusion coefficient of sodium ions remains relatively constant at >0.1 V, then falls
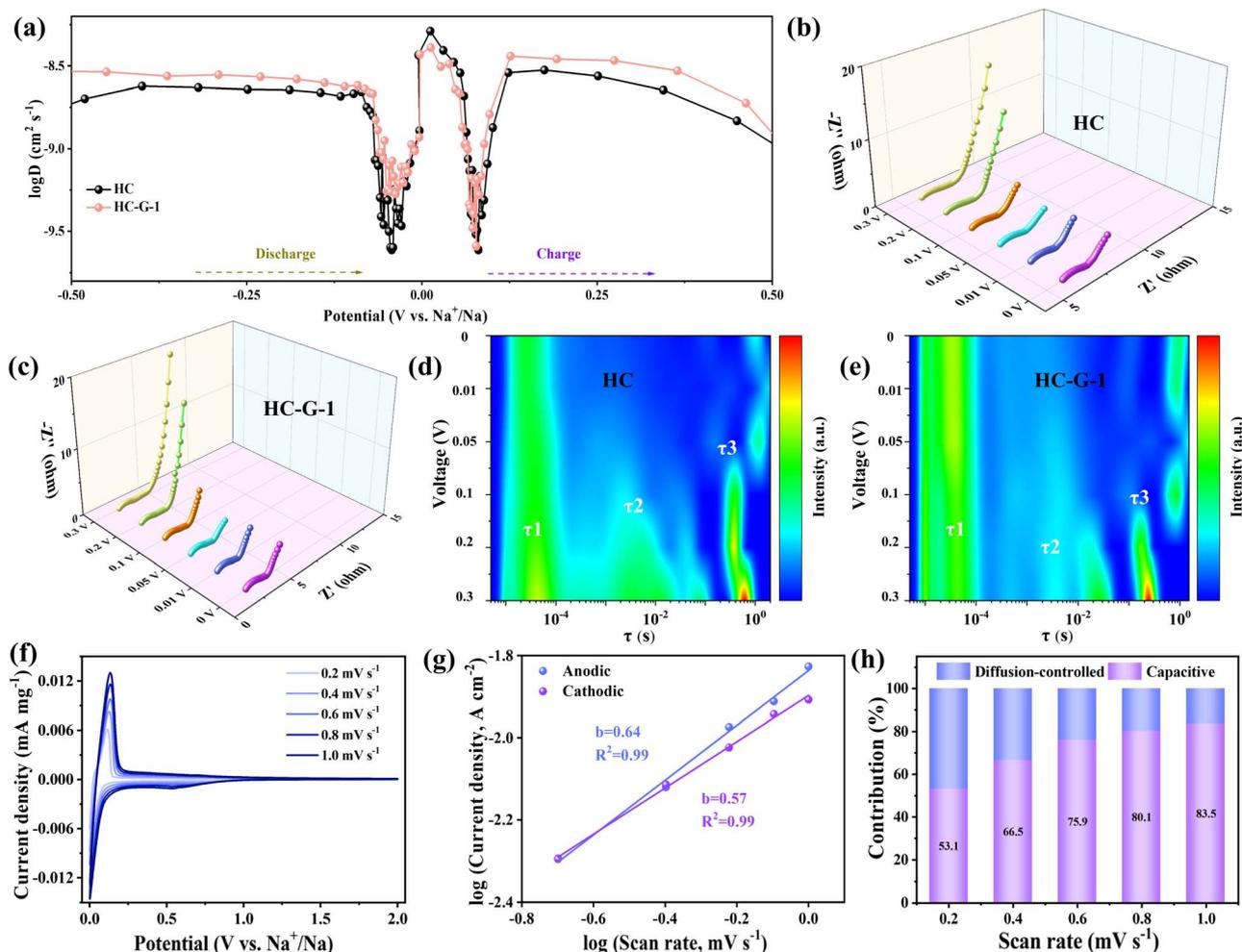
Fig. 4 The charge-storage kinetics analysis of the graphene orientation-induced cellulose-derived hard carbon series. (a) Estimated sodium ion diffusion coefficients from the GITT potential profiles of the HC and HC-G-1 electrodes for the sodiation/desodiation processes. (b and c) *In-situ* electrochemical impedance spectra (EIS) of the HC and HC-G-1 electrodes from 0.3 V to 0 V, and (d and e) corresponding to the different stages of the contour plots of DRTs ($\tau 1$, $\tau 2$, $\tau 3$) for the HC and HC-G-1 electrodes during the discharging process. (f and g) The CV curves of the HC-G-1 electrode at different scan rates and the contribution of capacitance. (h) The diffusion control charge at various scan rates of the HC-G-1 electrode.

sharply around 0.1 V and rises gradually after reaching a minimum near 0.05 V. It further indicates that the different sodium storage behaviors correspond to the region around 0.1 V. The diffusion coefficient of sodium ions is higher in the slope region than in the plateau region, suggesting that the plateau region is the main reason for the limited rate performance of hard carbon. Additionally, the low-voltage plateau region diffusion coefficient of the HC-G-1 electrode is obviously higher than that of the HC electrode, which is mainly attributed to the fact that the increase in closed pore size and pseudographitic domains can induce more sodium ions to rapidly enter the closed pore structure.[46] Meanwhile, a larger closed pore volume can also accommodate the rapid storage of sodium ions. In order to further investigate the sodium ion storage process in hard carbon, *in-situ* electrochemical impedance spectroscopy (EIS) tests were performed on the HC and HC-G-1 electrodes. Fig. 4b and c show the *in-situ* Nyquist plots of the HC

and HC-G-1 electrodes, where the impedance profiles are primarily composed of a high-frequency semicircle and a low-frequency straight line. The slope curve in the low-frequency region gradually increases as the discharge proceeds and almost disappears after 0.1 V, indicating that the diffusion control in the pores becomes the dominant mechanism. In addition, the overall impedance of the HC-G-1 electrode containing graphene is lower than that of the HC sample without graphene, which explains the better rate performance of the HC-G-1 sample. The distribution of relaxation times of HC and HC-G-1 electrodes is displayed in Fig. 4d, e and S11, SI. The curves are roughly divided into four regions, contact resistance ($\tau 1$), solid electrolyte interface film resistance ($\tau 2$), charge transfer resistance ($\tau 3$) and diffusion resistance ($\tau 4$).[47,48] The $\tau 1$ of the samples decreased distinctly as the discharge progressed, and the $\tau 2$ and $\tau 3$ also decreased and shifted as the voltage decreased. The total cell polarization of the HC-G-1 electrode

was lower than that of the HC electrode during the discharge process, indicating accelerated diffusion kinetics of sodium ions in the plateau region.

As shown in Fig. 4f, the scanning rate of the HC-G-1 electrode was sequentially increased from 0.2 mV s^{-1} to 1.0 mV s^{-1}, and a small difference in the peak positions of the redox peaks was observed, indicating a low degree of polarization. Benefiting from the outstanding pore structure of the HC-G-1 electrode, it helps reduce the de-embedding and transport energy barriers of sodium ions between the graphitic domains, thereby enhancing the rate performance. The relationship between current and sweep speed is further analyzed by using the formula of $i = av^b$. The b value was calculated to describe whether the electrode reaction process was surface-controlled or diffusion-controlled, where i represents the peak current and v represents the scanning rate.[49,50] The b-values obtained for the oxidation and reduction peaks are 0.57 and 0.64, respectively (Fig. 4g), indicating that the sodium storage mechanism of the HC-G-1

electrode is a combination of diffusion- and surface-controlled processes. The contribution proportions of different control processes were further calculated. With the increase of scan rates, the capacitive contribution proportions of the HC-G-1 electrode were 53.1, 66.5, 75.9, 80.1 and 83.5% at scan rates of 0.2, 0.4, 0.6, 0.8 and 1.0 mV s^{-1}, respectively (Fig. 4h), which forecasted that the capacitive contribution proportion increases with higher current density.

The sodium storage mechanism was assessed using the *in-situ* Raman spectra of the HC-G-1 electrode during the first discharge process (Fig. 5a). Two characteristic peaks of carbon materials are observed: the D band (~1350 cm^{-1}) associated with disordered sp^2-hybridized carbon (defects, edges, or amorphous domains) and the G band (~1580 cm^{-1}) corresponding to the in-plane vibration of ordered graphitic layers.[51] In the high-voltage slope region (0.8–0.1 V), the I_D/I_G ratio gradually decreases (Fig. S12, SI), which promotes the reconstruction of disordered regions (*e.g.*, defects and edges) on the
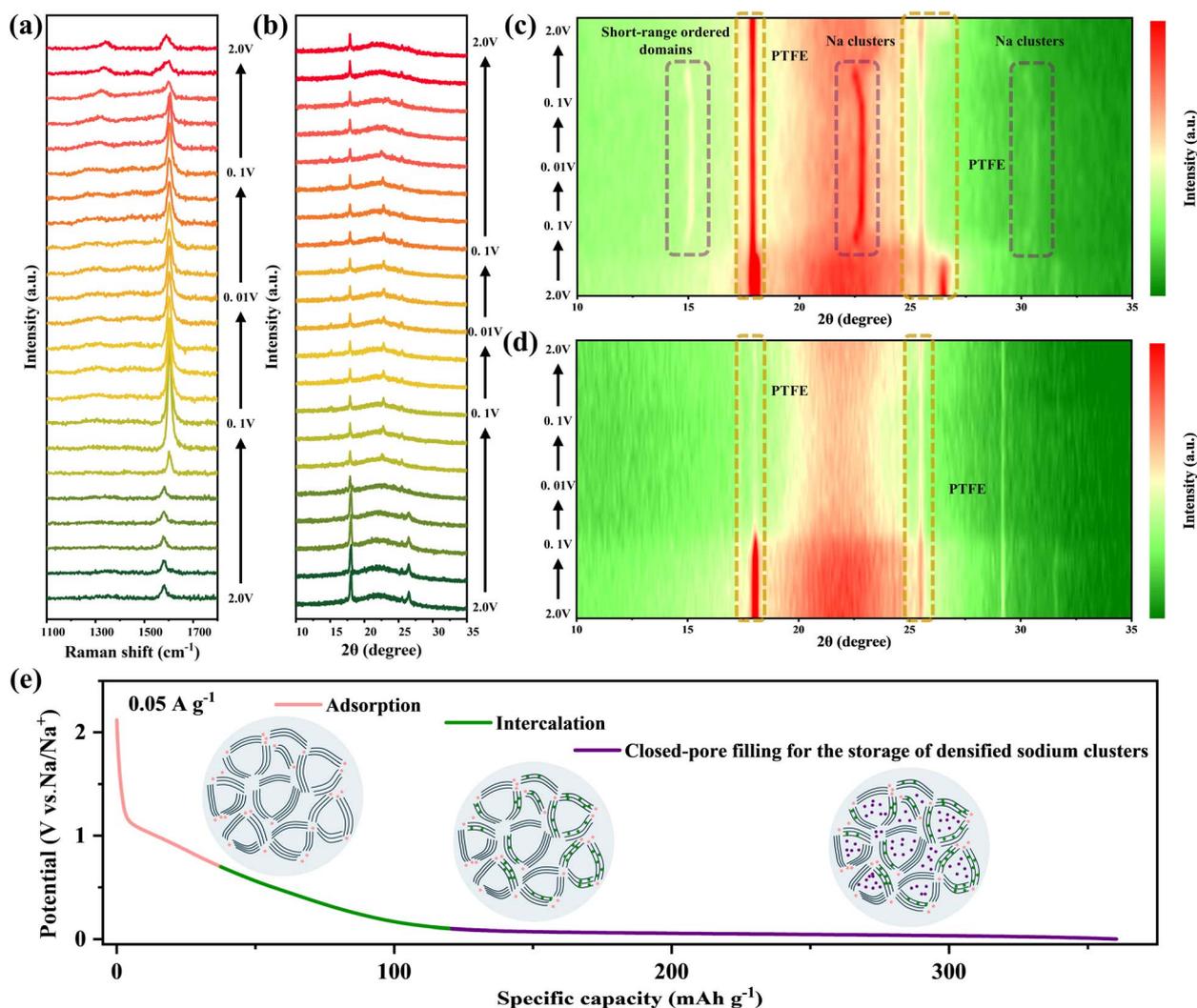

Fig. 5 Sodium storage mechanism of the graphene orientation-induced cellulose-derived hard carbon series. (a) *In-situ* Raman spectra, and (b) *in-situ* XRD patterns, and (c) corresponding the contour plots of the HC-G-1 sample during the first charge/discharge at a current density of 50 mA g^{-1}. (d) *In-situ* XRD patterns of the HC sample during the first charge/discharge at a current density of 50 mA g^{-1}. (e) Schematic diagram of the sodium storage mechanism of the HC-G-1 electrode.

hard carbon surface into graphitic domain structures, weakening the D band and relatively enhancing the G band. As discharge proceeds to the low-voltage plateau region (<0.1 V), the G band shifts upward by $\sim$10 cm^{-1} (from 1580 to 1590 cm^{-1} with a blue shift) accompanied by a slight narrowing. Notably, due to the stable structure and non-participation of graphene in redox reactions, it provides interlayer support to alleviate structural damage of hard carbon during sodium intercalation, preserving more ordered graphitic domains and remarkably enhancing the G band. Additionally, graphene mechanical support inhibits excessive interlayer expansion of hard carbon during sodium ion intercalation (preventing bond relaxation),[52] which raises the vibration frequency of the G band. This reversible structural evolution confirms that sodium ion deintercalation from graphitic layers and desorption from defects

are highly reversible processes, which underlies the stable cycling performance of the HC-G-1 sample. Notably, a minor hysteresis is observed in the I_D/I_G recovery ($\Delta I_D/I_G$ $\sim$0.05) (Fig. S13, SI), which may originate from residual sodium ions trapped in ultra-small micropores that are inaccessible during desodiation, as supported by closed pore size distribution analysis. The *in-situ* Raman results correlate directly with the sodium ion storage mechanism in the HC-G-1 electrode: surface adsorption on defects (slope region) induces negligible structural perturbation, and intercalation into graphitic layers and filling of micropores (plateau region) drive measurable changes in graphitic order and interlayer spacing.

We have also evaluated the structural stability of the HC-G-1 electrode by *in-situ* XRD (Fig. 5b). The position and full width at half maximum of the (002) peak show almost no obvious
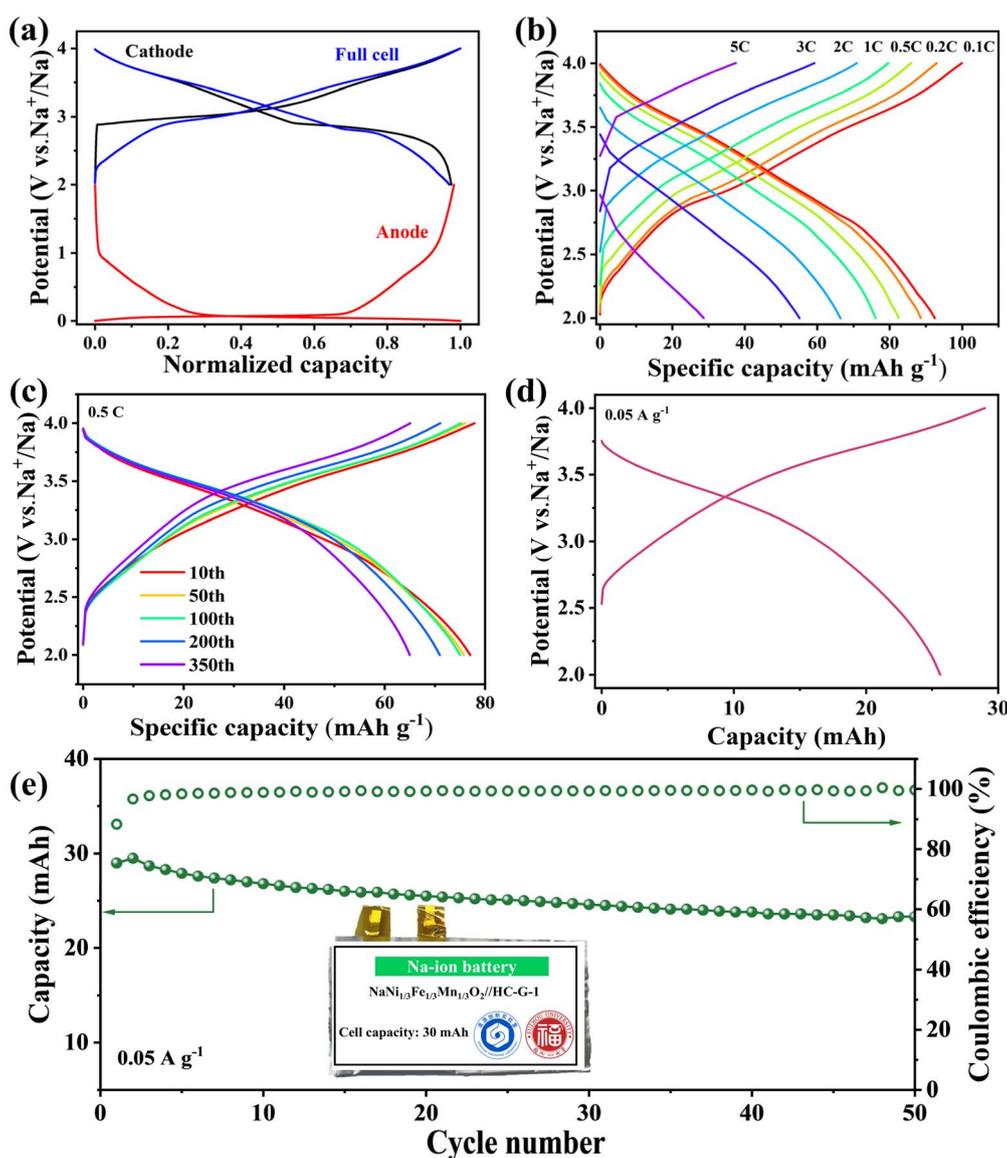

Fig. 6 (a) Initial discharge/charge curves of the NaNi$_{1/3}$Fe$_{1/3}$Mn$_{1/3}$O$_2$ cathode and the HC-G-1 anode at 0.02 A g^{-1}. (b) The discharge/charge curves of the NaNi$_{1/3}$Fe$_{1/3}$Mn$_{1/3}$O$_2$//HC-G-1 full-cell at different current densities (1C = 300 mA g^{-1}). (c) Cycling performance of the full-cell at a current density of 0.5 A g^{-1}. (d) The charge/discharge curves of the NaNi$_{1/3}$Fe$_{1/3}$Mn$_{1/3}$O$_2$//HC-G-1 pouch cell at a current density of 0.05 A g^{-1}, and (e) cycling performance of the assembled pouch cell at a current density of 0.05 A g^{-1}.

changes, which is mainly related to the fact that sodium ions in the slope region are mainly adsorbed on the surface defects (such as edges, vacancies) of hard carbon. With the increase of discharge depth in the plateau region (<0.1 V), the 15° diffraction peak corresponds to the diffraction signal of short-range ordered domains formed by the reversible rearrangement of local carbon structures. Additionally, diffraction peaks at 23.5° and 31° are observed in the plateau region, corresponding to the formation of quasi-sodium clusters (Fig. 5c).[53] Notably, Wu et al.[54] reported that a strong self-adsorption behavior leading to the formation of quasi-sodium metal clusters was detected in a rationally designed slope-type hard carbon anode based on highly defective ultrathin carbon nanosheets. However, due to the wide interlayer spacing of hard carbon that can accommodate the transport of sodium ions/clusters, conventional plateau-type hard carbon anodes fail to detect reversible sodium metal clusters during *in-situ* XRD measurements. This is not only the first observation of sodium metal cluster formation through *in-situ* XRD in the plateau-type hard carbon, but also strongly linked to the process of sodium ions/clusters primarily filling the ultra-small micropores of hard carbon. The peaks at 18° and 27° are the structural peaks of the PTFE binder. In addition, as the discharge proceeds, the concentration of sodium ions in the micropores continues to increase, and the Na clusters gradually grow (Fig. S14, SI), but the mechanical resistance of the micropore walls (ordered layers of hard carbon) limits the lateral expansion of the clusters. To adapt to the confined space, Na atoms are forced to stack in a more compact manner, resulting in a decrease in the internal interplanar spacing of the clusters (such as the (111) plane of Na), which is manifested as the shift of the diffraction peak to a higher angle.[55,56] During charging, sodium clusters decompose into sodium ions and undergo desodiation from the micropores. With the removal of constraints, the atomic spacing is restored, and the diffraction peak shifts back to its initial position. It confirms that graphene-induced hard carbon achieves stable formation and decomposition of sodium clusters through spatial confinement-densification regulation, which serves as the key guarantee for the capacity reversibility in the low-voltage plateau region. However, during the discharge process of the HC sample, the position of the (002) peak remains essentially unchanged in the slope region, while a slight shift occurs, reflecting the expansion of carbon layers under the extrusion of sodium clusters in the plateau region (Fig. 5d). Meanwhile, a broadened weak diffraction peak emerges at $2\theta \approx 23.5°$, corresponding to disorderly grown sodium clusters,[57] indicating that the sodium clusters are randomly agglomerated in the unconfined space. Therefore, these results demonstrate that the HC-G-1 electrode exhibits reversible and dense sodium metal clusters in the plateau region. Furthermore, the confined local graphitization induced by graphene runs through the three stages of sodium storage in hard carbon (Fig. 5e). It optimizes the orderliness of surface defects and improves adsorption stability in the adsorption stage. It regulates the interlayer spacing and ordered domains to enhance the reversibility of intercalation in the intercalation stage. It strengthens the spatial confinement of micropores to achieve controllable densification of sodium clusters in the filling stage.

To evaluate the potential of HC-G-1 for energy storage applications, a sodium-ion full cell was assembled with HC-G-1 as the anode and $NaNi_{1/3}Fe_{1/3}Mn_{1/3}O_2$ as the cathode (voltage window: 2.0–4.0 V, Fig. 6a and S15, SI). As depicted in Fig. 6b and S16, SI, the full cell delivers a reversible capacity of 92.7 mAh g^{-1} at 0.1C based on the active mass of the cathode electrode, benefiting from the optimized confined pore structure of HC-G-1 that mitigates irreversible sodium ion consumption. The $NaNi_{1/3}Fe_{1/3}Mn_{1/3}O_2$//HC-G-1 full cell retains a discharge capacity of 86.2 mAh g^{-1} under high-rate conditions of 0.5C (1C = 300 mA g^{-1}). Remarkably, long-term cycling tests reveal a capacity retention of 84.4% after 350 cycles at 0.5C (Fig. 6c), confirming that the excellent structural stability of the HC-G-1 electrode facilitates the storage of dense sodium metal clusters during repeated sodiation/desodiation. More importantly, to further validate its practical applicability, a pouch cell was fabricated with HC-G-1 as the anode and the same cathode (Fig. 6d). As shown in Fig. 6e, the pouch cell exhibits good stability with a capacity retention of 80.3% after 50 cycles, and holds promise for the commercialization of this material design approach in low-cost sodium-ion batteries for grid energy storage.

Conclusion

In summary, we demonstrate that nanoconfinement induction *via* graphene-oriented graphitization is a robust strategy to overcome the intrinsic limitations of cellulose-derived hard carbon anodes for sodium-ion batteries. Based on the dual roles of graphene in this strategy—cross-linking the structure to suppress disordered defects and inducing the directional arrangement of carbon layers *via* its sp^2-skeleton at high temperatures—a synergistic confined structure is constructed, characterized by abundant pseudo-graphitic domains, expanded interlayer spacing, and size-tunable closed pores. This confined structure balances sodium storage capacity and ion transport kinetics, addressing the key challenges of low ICE, insufficient capacity, and poor rate performance in traditional hard carbon. The optimized sample achieves excellent performance with a specific capacity of 323.9 mAh g^{-1}, an initial Coulombic efficiency of 89.9%, and a cycling retention rate of 80.2% after 1000 cycles. These improvements originate from the nanoconfinement-induced enhancement of the adsorption–intercalation–pore filling mechanism: optimized surface defect orderliness stabilizes sodium adsorption in the slope region, regulated interlayer spacing promotes reversible sodium intercalation, and strengthened micropore confinement enables controllable densification of sodium clusters, boosting the low-voltage plateau capacity to 216.4 mAh g^{-1}. *In-situ* characterization first reveals sodium metal cluster peaks (23.5°, 31°) *via* XRD and confirms reversible structural evolution *via* Raman spectroscopy. These insights not only advance designing high-performance hard carbon anodes, but also provide a general strategy for confined ion storage systems, speeding up the application of SIBs in large-scale energy storage.

Author contributions

Lian Chen: writing – original draft, methodology, investigation, data curation; Fan Li: software, investigation, validation, visualization; Kaiyang Liu: data curation, methodology; Feng Wang: conceptualization, data curation, investigation, writing – review and editing, project administration, funding acquisition; Zhengshuai Bai: data curation, writing – review and editing; Yanyan Zhang: formal analysis, supervision, writing – review and editing; Yuxin Tang: writing – review and editing, resources, supervision, project administration, and funding acquisition.

Conflicts of interest

There are no conflicts to declare.

Data availability

The data supporting this article have been included as part of the supplementary information (SI). Supplementary information: experimental details and results. See DOI: https://doi.org/10.1039/d5sc09998f.

Acknowledgements

References

1 A. Yao, S. M. Benson and W. C. Chueh, *Nat. Energy*, 2025, **10**, 404–416.

2 C. Zhao, Q. Wang, Z. Yao, J. Wang, B. Sánchez-Lengeling, F. Ding, X. Qi, Y. Lu, X. Bai, B. Li, H. Li, A. Aspuru-Guzik, X. Huang, C. Delmas, M. Wagemaker, L. Chen and Y.-S. Hu, *Science*, 2020, **370**, 708–711.

3 X. Wang, Q. Zhang, C. Zhao, H. Li, B. Zhang, G. Zeng, Y. Tang, Z. Huang, I. Hwang, H. Zhang, S. Zhou, Y. Qiu, Y. Xiao, J. Cabana, C.-J. Sun, K. Amine, Y. Sun, Q. Wang, G.-L. Xu, L. Gu, Y. Qiao and S.-G. Sun, *Nat. Energy*, 2024, **9**, 184–196.

4 M. Wu, J. Liao, L. Yu, R. Lv, P. Li, W. Sun, R. Tan, X. Duan, L. Zhang, F. Li, J. Kim, K. H. Shin, H. Seok Park, W. Zhang, Z. Guo, H. Wang, Y. Tang, G. Gorgolis, C. Galiotis and J. Ma, *Chem.–Asian J.*, 2020, **15**, 995–1013.

5 F. Wang, Z. Jiang, Y. Zhang, Y. Zhang, J. Li, H. Wang, Y. Jiang, G. Xing, H. Liu and Y. Tang, *eScience*, 2024, **4**, 100181.

6 Y. Li, A. Vasileiadis, Q. Zhou, Y. Lu, Q. Meng, Y. Li, P. Ombrini, J. Zhao, Z. Chen, Y. Niu, X. Qi, F. Xie, R. van der Jagt, S. Ganapathy, M.-M. Titirici, H. Li, L. Chen, M. Wagemaker and Y.-S. Hu, *Nat. Energy*, 2024, **9**, 134–142.

7 M. Yuan, H. Wang, T. Xu, N. Chu, D. Kong, L. Zeng, Y. Wang, X. Bai and H. Seok Park, *Angew. Chem., Int. Ed.*, 2025, **64**, e202417930.

8 L. Chen, F. Li, F. Wang, Z. Bai, Y. Zhang and Y. Tang, *Adv. Funct. Mater.*, 2025, e19895.

9 B. Pei, H. Yu, L. Zhang, G. Fang, J. Zhou, X. Cao and S. Liang, *Adv. Mater.*, 2025, **37**, 2504574.

10 F. Wang, L. Chen, J. Wei, C. Diao, F. Li, C. Du, Z. Bai, Y. Zhang, O. I. Malyi, X. Chen, Y. Tang and X. Bao, *Energy Environ. Sci.*, 2025, **18**, 4312–4323.

11 H. Ma, Y. Tang, B. Tang, Y. Zhang, L. Deng, L. Liu, S. Dong and Y. Cao, *Carbon Energy*, 2024, **6**, e584.

12 Z. Hou, W. He, F. Wu, Y. Du, F. Xu and J.-G. Wang, *Energy Storage Mater.*, 2025, **80**, 104455.

13 F. Wang, F. Li, H. Gong, Y. Zhang, X. Liu, Z. Jiang, L. Chen, J. Huang, Y. Zhang, Y. Jiang, B. Chen and Y. Tang, *J. Alloys Compd.*, 2024, **981**, 173668.

14 S. You, Q. Zhang, J. Liu, Q. Deng, Z. Sun, D. Cao, T. Liu, K. Amine and C. Yang, *Energy Environ. Sci.*, 2024, **17**, 8189–8197.

15 N. Lan, Y. Shen, J. Li, H. He and C. Zhang, *Adv. Mater.*, 2025, **37**, 2412989.

16 F. Wang, J. Lee, L. Chen, G. Zhang, S. He, J. Han, J. Ahn, J. Y. Cheong, S. Jiang and I.-D. Kim, *ACS Nano*, 2023, **17**, 8866–8898.

17 X. Feng, Y. Li, Y. Li, M. Liu, L. Zheng, Y. Gong, R. Zhang, F. Wu, C. Wu and Y. Bai, *Energy Environ. Sci.*, 2024, **17**, 1387–1396.

18 J. M. Stratford, A. K. Kleppe, D. S. Keeble, P. A. Chater, S. S. Meysami, C. J. Wright, J. Barker, M.-M. Titirici, P. K. Allan and C. P. Grey, *J. Am. Chem. Soc.*, 2021, **143**, 14274–14286.

19 Q. Li, X. Liu, Y. Tao, J. Huang, J. Zhang, C. Yang, Y. Zhang, S. Zhang, Y. Jia, Q. Lin, Y. Xiang, J. Cheng, W. Lv, F. Kang, Y. Yang and Q.-H. Yang, *Natl. Sci. Rev.*, 2022, **9**, nwac084.

20 Z. Lu, H. Yang, Y. Guo, H. Lin, P. Shan, S. Wu, P. He, Y. Yang, Q.-H. Yang and H. Zhou, *Nat. Commun.*, 2024, **15**, 3497.

21 Y. Zhang, S.-W. Zhang, Y. Chu, J. Zhang, H. Xue, Y. Jia, T. Cao, J. Qiu, X. Zou, D.-W. Wang, Y. Tao, G. Zhong, Z. Peng, F. Kang, W. Lv and Q.-H. Yang, *Nat. Commun.*, 2025, **16**, 3634.

22 J. Zheng, C. Guan, H. Li, D. Wang, Y. Lai, S. Li, J. Li and Z. Zhang, *Adv. Energy Mater.*, 2024, **14**, 2303584.

23 W. Bai, H. Wang, D. H. Min, J. Miao, B. Li, T. Xu, D. Kong, X. Li, X. Yu, Y. Wang and H. S. Park, *Adv. Sci.*, 2024, **11**, 2404419.

24 F. Wang, L. Zhang, Q. Zhang, J. Yang, G. Duan, W. Xu, F. Yang and S. Jiang, *Appl. Energy*, 2021, **289**, 116734.

25 J. Liu, L. Huang, H. Wang, L. Sha, M. Liu, Z. Sun, J. Gu, H. Liu, J. Zhao, Q. Zhang and L. Zhang, *Electrochem. Energy Rev.*, 2024, **7**, 34.

26 P. Z. Xiao, Z. Li, Y. Sun, F. Zheng, C. Xu, D. Sun, S. Liu, B. Sun, Z. Wang, S. Liao, T. Pan, Q. Ye, T. Li, P. C. Xu and P. Y. Li, *Energy Storage Mater.*, 2025, **78**, 104283.

27 H. Liu, X. Huang, Y. Wang, B. Kuang and W. Li, *Nat. Commun.*, 2024, **15**, 164.

28 Z. Yang, Y. Zhang, H. Zhou, M. Cui, Y. Zhong, T. Hu, Q. Wang and C. Meng, *Carbon Neutralization*, 2025, **4**, e70057.

29 F. Wang, J. Y. Cheong, Q. He, G. Duan, S. He, L. Zhang, Y. Zhao, I.-D. Kim and S. Jiang, *Chem. Eng. J.*, 2021, **414**, 128767.

30 M. Song, Q. Song, T. Zhang, X. Huo, Z. Lin, Z. Hu, L. Dong, T. Jin, C. Shen and K. Xie, *Nano Res.*, 2023, **16**, 9299–9309.

31 Z. Hou, Y. Zhao, Y. Du, F. Wu, W. He, F. Xu and J.-G. Wang, *Adv. Funct. Mater.*, 2025, **35**, 2505468.

32 H. Zhang, Z. Huang, S. Lin, J. Cui, Q. Zhang, X. Luo, R. Wang, C. Zhang, C. Shu and W. Tang, *Chem. Sci.*, 2025, **16**, 16678–16689.

33 L. Kitsu Iglesias, E. N. Antonio, T. D. Martinez, L. Zhang, Z. Zhuo, S. J. Weigand, J. Guo and M. F. Toney, *Adv. Energy Mater.*, 2023, **13**, 2302171.

34 D. Saurel, J. Segalini, M. Jauregui, A. Pendashteh, B. Daffos, P. Simon and M. Casas-Cabanas, *Energy Storage Mater.*, 2019, **21**, 162–173.

35 Y. Xue, Y. Chen, Y. Liang, L. Shi, R. Ma, X. Qiu, Y. Li, N. Guo, Q. Zhuang, B. Xi, Z. Ju and S. Xiong, *Adv. Mater.*, 2025, **37**, 2417886.

36 X. Chen, N. Sawut, K. Chen, H. Li, J. Zhang, Z. Wang, M. Yang, G. Tang, X. Ai, H. Yang, Y. Fang and Y. Cao, *Energy Environ. Sci.*, 2023, **16**, 4041–4053.

37 Y. Lu, Y. Lu, Z. Niu and J. Chen, *Adv. Energy Mater.*, 2018, **8**, 1702469.

38 Z. Mao, R. Wang, B. He, J. Jin, Y. Gong and H. Wang, *Small*, 2023, **19**, 2207224.

39 W.-Y. Qian, X.-Y. Zhou, X.-Y. Liu, M.-Y. Su, K.-Y. Zhang and X.-L. Wu, *Chem. Sci.*, 2025, **16**, 104–112.

40 Z. Huang, J. Huang, L. Zhong, W. Zhang and X. Qiu, *Small*, 2024, **20**, 2405632.

41 Y. Wang, Z. Yi, L. Xie, Y. Mao, W. Ji, Z. Liu, X. Wei, F. Su and C.-M. Chen, *Adv. Mater.*, 2024, **36**, 2401249.

42 C. Wu, Y. Yang, Y. Zhang, H. Xu, W. Huang, X. He, Q. Chen, H. Dong, L. Li, X. Wu and S. Chou, *Angew. Chem., Int. Ed.*, 2024, **63**, e202406889.

43 C. Li, Q. Chen, Y. Zhang, P. Zhao, X. He, Q. Gu, J. Wang, S.-L. Chou and X. Wu, *Energy Storage Mater.*, 2025, **82**, 104580.

44 Z. Yu, X. Li, N. Sun, H. Chen, R. A. Soomro and B. Xu, *Energy Storage Mater.*, 2025, **82**, 104612.

45 Z.-G. Liu, J. Zhao, H. Yao, X.-X. He, H. Zhang, Y. Qiao, X.-Q. Wu, L. Li and S.-L. Chou, *Chem. Sci.*, 2024, **15**, 8478–8487.

46 Y. Morikawa, S. i. Nishimura, R. i. Hashimoto, M. Ohnuma and A. Yamada, *Adv. Energy Mater.*, 2019, **10**, 1903176.

47 Y. Lu, C.-Z. Zhao, J.-Q. Huang and Q. Zhang, *Joule*, 2022, **6**, 1172–1198.

48 Y. Lu, C.-Z. Zhao, R. Zhang, H. Yuan, L.-P. Hou, Z.-H. Fu, X. Chen, J.-Q. Huang and Q. Zhang, *Sci. Adv.*, 2021, **7**, eabi5520.

49 F. Wang, X. Liu, G. Duan, H. Yang, J. Y. Cheong, J. Lee, J. Ahn, Q. Zhang, S. He, J. Han, Y. Zhao, I. D. Kim and S. Jiang, *Small*, 2021, **17**, 2102532.

50 L. Chen, F. Wang, Z. Tian, H. Guo, C. Cai, Q. Wu, H. Du, K. Liu, Z. Hao, S. He, G. Duan and S. Jiang, *Small*, 2022, **18**, 2201307.

51 F. Wang, J. Y. Cheong, J. Lee, J. Ahn, G. Duan, H. Chen, Q. Zhang, I. D. Kim and S. Jiang, *Adv. Funct. Mater.*, 2021, **31**, 2101077.

52 Q. Xiao, W. Li, S. Xie, L. Wang and C. Y. Tang, *Nat. Commun.*, 2024, **15**, 9607.

53 Z. Wang, X. Feng, Y. Bai, H. Yang, R. Dong, X. Wang, H. Xu, Q. Wang, H. Li, H. Gao and C. Wu, *Adv. Energy Mater.*, 2021, **11**, 2003854.

54 X. Liu, M. Zhang, X. Wang, Y. Peng, Y. Liu, S. Ullah, Z. Duan, W. Gao, B. Song, M. Wei, J. He, Z. Li and Y. Wu, *Adv. Mater.*, 2025, **37**, 2410673.

55 M. Anji Reddy, M. Helen, A. Groß, M. Fichtner and H. Euchner, *ACS Energy Lett.*, 2018, **3**, 2851–2857.

56 Y. Aniskevich, J. H. Yu, J.-Y. Kim, S. Komaba and S.-T. Myung, *Adv. Energy Mater.*, 2024, **14**, 2304300.

57 S.-J. Jiang, Y.-S. Xu, X.-W. Sun, L. Chen, Y.-N. Li, L. Li and F.-F. Cao, *J. Am. Chem. Soc.*, 2025, **147**, 8088–8092.